The Convection of a Bingham Fluid in a Differentially-Heated Porous Cavity

D. Andrew S. Rees

Department of Mechanical Engineering, University of Bath, Bath BA2 7AY, UK.

✉ D.A.S.Rees@bath.ac.uk

Abstract

Purpose – The purpose is to determine the manner in which a yield-stress fluid begins convecting when it saturates a porous medium. A sidewall-heated rectangular cavity is selected as the testbed for this pioneering work.

Design/methodology/approach – Steady solutions are obtained using (i) a second-order accurate finite difference method, (ii) line relaxation based on the Gauss-Seidel smoother, (iii) a Full Approximation Scheme multigrid algorithm with V-cycling and (iv) a regularization of the Darcy-Bingham model to smooth the piecewise linear relation between the Darcy flux and the applied body forces.

Findings – While Newtonian fluids always convect whenever the Darcy-Rayleigh number is nonzero, Bingham fluids are found to convect only when the Darcy-Rayleigh number exceeds a value which is linearly dependent on both the Rees-Bingham number and the overall perimeter of the rectangular cavity. Stagnation is always found in the centre of the cavity and in regions close to the four corners. Care must be taken over the selection of the regularization constant.

Research limitations/implications – The Darcy-Rayleigh number is restricted to values which are at or below 200.

Originality/value – This is the first investigation of the effect of yield stress on nonlinear convection in porous media.

Keywords – Porous media, convection, stagnation, nonlinear flow, rectangular cavity, Bingham fluid.

Paper type – Research paper.

Nomenclature

c	regularization constant
g	gravity
G	threshold pressure gradient
h	microchannel width
H	height of the cavity
K	permeability
L	width of the cavity
Nu	Nusselt number
p	pressure
q	fluid speed ($\sqrt{u^2+w^2}$)
Ra	Darcy-Rayleigh number
Rb	Rees-Bingham number
T	dimensional temperature
u	horizontal velocity
w	vertical velocity
x	horizontal coordinate
z	vertical coordinate

Greek symbols

α	diffusivity
β	expansion coefficient
θ	nondimensional temperature
μ	dynamic viscosity
τ_0	yield stress
ρ	reference density
ψ	streamfunction

Subscripts, superscripts, and other symbols

c	cold
h	hot
x	derivative with respect to x
z	derivative with respect to z

1 Introduction

Yield-stress fluids are surprisingly ubiquitous, appearing as they do in very many aspects of daily life and the environment. Examples include sewage sludges, magma, marine sediments, various foodstuffs such as yoghurt, purées and mayonnaise, and fluids in the oil industry such as drilling muds, heavy oils and surfactants (see Shenoy 1991, Barnes 1999, Sochi and Blunt 2008, Liu et al. 2012, Jeong 2013, and Maßmeyer 2013). The simplest one is a Bingham fluid where the rate of strain is a piecewise-linear function of the shear stress. When the magnitude of the shear stress is below the yield stress, then the rate of strain is zero and either the fluid is stationary or else is moving as a seemingly solid plug.

While a large and mature literature is associated with yield-stress fluids in general, once those fluids saturate a porous medium there are far fewer studies available. While undertaking a detailed literature review for Rees (2015a) it was found that there are only about a dozen papers dealing with convection of yield-stress fluids in a porous medium and all considered flow of boundary layer type in an otherwise unbounded region; see Rees (2015b) for comments on the realizability of the flows described in these papers. Therefore the literature is silent on the topic of cavity convection of a Bingham fluid in porous media.

One aim of the present paper, then, is to consider how the presence of a yield threshold alters the well-known manner in which convection takes place in a sidewall-heated porous cavity. This is an excellent testbed for a first study because such cavities, and indeed sidewall-heated vertical channels, are known to have unique solutions even when the Darcy-Rayleigh number is very large (Gill 1969, Lewis et al. 1995), and therefore numerical solutions are unencumbered by the need to determine stability criteria. The resulting flow generally takes the form of one recirculating cell, with boundary layers developing on all four surfaces when the Darcy-Rayleigh number becomes sufficiently large (Blythe et al. 1982, 1983). Other authors have used this cavity for similar purposes and their work includes the following topics/effects: layering (Lai and Kulacki 1988), local thermal nonequilibrium (Baytaş and Pop 2002), form drag (Saeid and Pop 2005), the presence of a nanofluid (Celli 2013) and variable permeability (Fahs et al. 2015).

When attempting to compute the flow of yield-stress the chief difficulty is that of the determination of the yield surface so that the fluid either side of that surface may be modelled in the appropriate manner.

For clear fluids (i.e. where no porous matrix is present) two approaches have been used to circumvent this difficulty. One is the biviscosity model (O'Donovan and Tanner 1984) where the viscosity is set to a large constant value whenever the shear stress is below the yield stress. The other is a regularization which is effectively a smooth version of the biviscosity model (Papanastasiou 1987 — used recently in Turan et al. 2011, 2014). When a Bingham fluid saturates a porous medium the yield stress is replaced by a yield body force, such as the pressure gradient, but the same numerical difficulties arise. We will therefore propose a suitable regularization for flows in porous media. Given that the computation of convective flows of yield-stress fluids is a novel topic, the secondary aim of the present paper is to establish a suitable protocol for undertaking this task accurately. Consequently our analysis is quite detailed and thorough.

2 Governing Equations and Numerical Method

2.1 The Darcy-Bingham law.

It is important at the outset to make clear the assumptions and restrictions behind the governing equations for the flow of a Bingham fluid within a porous medium. We begin with the experimental observation of Pascal (1981) that, for isothermal unidirectional flow in a porous medium, Darcy's law must be modifed by the presence of a threshold above which flow may occur. Thus for steady flows we have what shall be termed here the Darcy-Bingham law,

$$u = \begin{cases} -\dfrac{K}{\mu}\Big[1 - \dfrac{G}{|p_x|}\Big]p_x & \text{when } |p_x| > G, \\ 0 & \text{otherwise,} \end{cases} \tag{1}$$

where the value, G, is the threshold pressure gradient. If a porous medium were to be composed of a parallel set of identical channels of width, h, then Rees (2015a) shows that the threshold gradient is given by $G = 2\tau_0/h$ where τ_0 is the yield stress of the fluid. An almost identical formula for G applies when the microstructure is composed of tubes of circular cross-section. In such cases the equation which replaces Eq. (1) is a scaled form of the well-known Buckingham-Reiner law (Buckingham 1921). In this case, once the applied pressure gradient exceeds the threshold value, the induced flow first increases quadratically and eventually becomes linear. In the present paper we will not consider this more complicated relation, but will confine our attention to the above Darcy-Bingham law.

Rees (2015a), quoting Nash (2013), also shows that a porous medium which consists of a square network of such channels is quite strongly anisotropic in its response to driving pressure gradients, even though this is an isotropic configuration for Newtonian fluids, and that the magnitude and direction of the resulting flow depends on the orientation of the pressure gradient relative to the channel network. Currently unpublished work by the present author shows that the degree of anisotropy is reduced substantially for the case of a network of channels at mutual angles of 60°. Consequently we would expect a random medium to be roughly isotropic, and therefore we need to extend Eq. (1) to the following frame-invariant two-dimensional form:

$$\begin{pmatrix} u \\ w \end{pmatrix} = \begin{cases} -\dfrac{K}{\mu}\Big[1 - \dfrac{G}{(p_x^2 + p_z^2)^{1/2}}\Big]\begin{pmatrix} p_x \\ p_z \end{pmatrix} & \text{when } (p_x^2 + p_z^2)^{1/2} > G, \\ \begin{pmatrix} 0 \\ 0 \end{pmatrix} & \text{otherwise,} \end{cases} \tag{2}$$

If we now have buoyancy acting in the vertical (z) direction, then buoyancy forces may be included easily

in the same way as pressure gradients are since both are body forces. Equation (2) becomes,

$$\begin{pmatrix} u \\ w \end{pmatrix} = \begin{cases} -\dfrac{K}{\mu}\Big[1 - \dfrac{G}{\sqrt{p_x^2 + (p_z - \rho g\beta(T-T_c))^2}}\Big] \begin{pmatrix} p_x \\ p_z - \rho g\beta(T-T_c) \end{pmatrix} & \text{when } \sqrt{p_x^2 + (p_z - \rho g\beta(T-T_c))^2} > G, \\ \begin{pmatrix} 0 \\ 0 \end{pmatrix} & \text{otherwise.} \end{cases} \tag{3}$$

It is assumed here that the Boussinesq approximation is valid and that density is a linear function of temperature. For convective flows we may complete the dimensional system of equations by stating both the equation of continuity,

$$u_x + w_z = 0, \tag{4}$$

and the steady heat transport equation,

$$uT_x + wT_z = \alpha(T_{xx} + T_{zz}). \tag{5}$$

We will be considering convection in a rectangular cavity with height, H, and length, L, and we define $A = L/H$ to be the aspect ratio. The above equations may now be nondimensionalized using the following transformations,

$$(x, z) \to H(x, z), \qquad (u, w) \to \frac{\alpha}{H}(u, w), \qquad p \to \frac{\mu\alpha}{K}p, \qquad T = T_c + \theta(T_h - T_c). \tag{6}$$

The governing equations now become,

$$u_x + w_z = 0, \tag{7}$$

$$\begin{pmatrix} u \\ w \end{pmatrix} = \begin{cases} -\Big[1 - \dfrac{\mathrm{Rb}}{\sqrt{p_x^2 + (p_z - \mathrm{Ra}\,\theta)^2}}\Big] \begin{pmatrix} p_x \\ p_z - \mathrm{Ra}\,\theta \end{pmatrix} & \text{when } \sqrt{p_x^2 + (p_z - \mathrm{Ra}\,\theta)^2} > \mathrm{Rb}, \\ \begin{pmatrix} 0 \\ 0 \end{pmatrix} & \text{otherwise.} \end{cases} \tag{8}$$

$$uT_x + wT_z = T_{xx} + T_{zz}. \tag{9}$$

The two nondimensional governing parameters which have appeared are the Darcy-Rayleigh and the Rees-Bingham numbers which are defined as,

$$\mathrm{Ra} = \frac{\rho g\beta K H(T_h - T_c)}{\mu\alpha}, \qquad \mathrm{Rb} = \frac{GKH}{\mu\alpha}. \tag{10}$$

The latter is a scaled threshold gradient which is suitable for convective flows (because of the presence of α) in porous media (because of K).

2.2 The regularized form of the Darcy-Bingham law.

In their present form, Eqs. (7)-(9) are exceptionally difficult to solve. First, it will be essential to locate the yield surface. Second, the usual elimination of pressure to produce the streamfunction/temperature formulation of the equations of motion is mathematically impossible. Therefore we will reformulate the Darcy-Bingham law using the idea of regularization which was first used by Papanastasiou (1987) in the context of the isothermal flows of a Bingham fluid without the presence of a porous matrix. The nondimensional form of Eq. (1) is

$$u = \begin{cases} -\Big[1 - \dfrac{\mathrm{Rb}}{|p_x|}\Big]p_x & \text{when } |p_x| > \mathrm{Rb}, \\ 0 & \text{otherwise,} \end{cases} \tag{11}$$

and the regularized form which we propose to use is,

$$u + \mathrm{Rb}\,\tanh(cu/\mathrm{Rb}) = -p_x, \tag{12}$$

where c is termed the regularization constant. Equations (11) and (12) look very different: while Eq. (11) gives u as a nonlinear function of p_x, Eq. (12) gives p_x as a nonlinear function of u which will then allow for a straightforward derivation of an equation for the streamfunction for two-dimensional simulations after eliminating the pressure terms.

Sketches of the Darcy-Bingham law and its regularization are given in Fig. 2. The diagonal line through the origin is Darcy's law (i.e. Eq. (11) with Rb = 0), and the dashed line is the Darcy-Bingham law (Eq. (11)) where one sees that no flow is induced whenever $-\mathrm{Rb} < p_x < \mathrm{Rb}$. The regularized Darcy-Bingham law (12) is illustrated for the case $c = 5$. As c increases, the dashed line mimics increasingly closely the threshold law. Within the range, $-\mathrm{Rb} < p_x < \mathrm{Rb}$, this curve tends towards the horizontal as c increases, and we could interpret this as a much increased viscosity within that range. Thus, when p_x is small, we may say that the effective viscosity is (1+c) times that when p_x is large, a result which follows immediately from a small-u expansion of Eq. (12). When c is sufficiently large, the threshold model is approximated well in both the stagnant and strongly-flowing regions with a local curved section to soften the corner in the Darcy-Bingham law where there is a sudden change in the gradient.

The extension of Eq. (12) to an isotropic law in two dimensions with the inclusion of buoyancy effects is now,

$$u\Big[1 + \mathrm{Rb}\,\frac{\tanh(cq/\mathrm{Rb})}{q}\Big] = -p_x, \tag{13}$$

$$w\Big[1 + \mathrm{Rb}\,\frac{\tanh(cq/\mathrm{Rb})}{q}\Big] = -p_z + \mathrm{Ra}\,\theta, \tag{14}$$

where $q^2 = u^2 + w^2$. These two equations replace Eqs. (8). Of course, this approach may also be used for three-dimensional simulations.

We may now eliminate p from the momentum equations and introduce the streamfunction, ψ, according to

$$u = -\psi_z, \qquad w = \psi_x. \tag{15}$$

Equation (7) is satisfied immediately, while the heat transport equation, (9), becomes,

$$\theta_{xx} + \theta_{zz} = \psi_x\theta_z - \psi_z\theta_x. \tag{16}$$

Finally, Eqs. (13) and (14) combine to become,

$$\nabla^2\psi + \frac{\mathrm{Rb}\,\tanh(cq/\mathrm{Rb})}{q^3}\Big[\psi_z^2\psi_{xx} - 2\psi_x\psi_z\psi_{xz} + \psi_x^2\psi_{zz}\Big] + \frac{c\,\mathrm{sech}^2(cq/\mathrm{Rb})}{q^2}\Big[\psi_x^2\psi_{xx} + 2\psi_x\psi_z\psi_{xz} + \psi_z^2\psi_{zz}\Big] = \mathrm{Ra}\,\theta_x, \tag{17}$$

where

$$q^2 = \psi_x^2 + \psi_z^2. \tag{18}$$

2.3 Numerical considerations.

We are considering convection within in a rectangular cavity with aspect ratio, A, with sidewall heating and cooling, and with insulated upper and lower surfaces. In nondimensional terms the boundary conditions are

$$\psi = 0, \quad \theta = 1 \quad \text{on} \quad x = 0; \qquad \psi = 0, \quad \theta = 0 \quad \text{on} \quad x = A; \qquad \psi = 0, \quad \theta_z = 0 \quad \text{on} \quad z = 0, 1, \tag{19}$$

and the cavity itself is sketched in Fig. 1.

Figure 1 near here

Equations (16) and (17) were discretized using standard second order accurate central difference approximations for all terms. The Neumann boundary conditions for θ given in Eq. (19) were approximated using a fictitious point method, thereby preserving second order accuracy. The discretized equations were then solved using a Gauss-Seidel iteration scheme employing line-relaxation as the basic smoother and this was accelerated using the Full Approximation Scheme multigrid methodology with V-cycling. Line relaxation was used because of the variable coefficients of ψ_{xx} and ψ_{zz} in Eq. (17), and it was applied in each coordinate direction alternately.

While the heat transport equation offers no numerical difficulties over and above what might normally be encountered when solving for a Newtonian fluid, the terms in the denominators in Eq. (17) suggest that one might encounter singular coefficents as $q \to 0$. This turns out not to happen but there is nevertheless-increasingly poor numerical conditioning as q gets smaller. If we assume that all velocities are small then all derivatives of ψ are also small and a Taylor's series expansion of (17) takes the following form,

$$\begin{aligned} & \Big[1 + c\left\{1 - \frac{1}{3}\Big(\frac{cq}{\mathrm{Rb}}\Big)^2 + \frac{2}{15}\Big(\frac{cq}{\mathrm{Rb}}\Big)^4 - \frac{17}{315}\Big(\frac{cq}{\mathrm{Rb}}\Big)^6 + \frac{62}{2835}\Big(\frac{cq}{\mathrm{Rb}}\Big)^8 + \cdots\right\}\Big]\nabla^2\psi \\ + \quad & \frac{c^3}{\mathrm{Rb}^3}\Big[-\frac{2}{3} + \frac{8}{15}\Big(\frac{cq}{\mathrm{Rb}}\Big)^2 - \frac{34}{105}\Big(\frac{cq}{\mathrm{Rb}}\Big)^4 + \frac{496}{2835}\Big(\frac{cq}{\mathrm{Rb}}\Big)^6 + \cdots\Big]\left[\psi_{xx}\psi_x^2 + 2\psi_x\psi_z\psi_{xz} + \psi_{zz}\psi_z^2\right] \qquad (20) \\ = \quad & \mathrm{Ra}\,\theta_x. \end{aligned}$$

Therefore, at leading order in q, the momentum equation reduces to

$$(1 + c)\nabla^2\psi = \mathrm{Ra}\,\theta_x, \qquad (21)$$

showing once more that the effective viscosity in this weak-flow regime is $(1 + c)$ times the post-threshold value. In practice, we solved Eq. (17) whenever $q > 10^{-4}$ and Eq. (20) when $q < 10^{-4}$. The number of expansion terms used in (20), even with the number of significant figures used by double precision `FORTRAN`, meant that there was a seamless transition between the two formulae as q crossed the 10^{-4} 'barrier'.

Detailed comments and reasons are given in the Appendix, but generally we used a steplength of 1/96 for our computations, and c took values which were at or above 40, thereby ensuring that the regularized form of the Darcy-Bingham law was always quite accurate. In general we found that 3 multigrid levels gave the most robust convergence: fewer levels increased the number of iterations required for convergence, while a larger number sometimes meant that the algorithm diverged. Convergence to the steady state was then deemed to have occurred once the maximum residual for Eq. (16) was below 10^{-7}.

3 Results and Discussion

Our numerical results are presented in two forms. First we display how the presence of the yield threshold modifies the velocity and temperature fields from those corresponding to a Newtonian fluid, with particular emphasis on the size and location of the ensuing stagnation regions, and second, we show the variations in the maximum streamfunction (i.e. the amount of fluid which convects around the cavity) and the Nusselt number across the cavity. The spatial extent of the stagnation regions is found by reference to Fig. 2. In that diagram the range of values of the pressure gradient for which the fluid ought to be stagnant using the Darcy-Bingham law is from $-\mathrm{Rb}$ to $+\mathrm{Rb}$. The orange disks in Fig. 2 indicate those two velocities which correspond to $p_x = \pm\mathrm{Rb}$ using the regularized model. Stagnation is then defined to correspond to where q lies between that range of velocities, and therefore such regions of deemed stagnation are shaded in orange in our contour plots.

Figure 2 near here

3.1 Typical streamlines, isotherms and stagnation regions

Our summary of the effect of the presence of a yield threshold on free convection in a sidewall-heated cavity is given in Figs. 3 to 7. In general we use the value, $c = 100$, in the regularised Darcy-Bingham model. Figures 3 and 4 correspond to the unit cavity with $A = 1$. In Fig. 3 we have taken $\mathrm{Ra} = 100$ and increased the value of Rb from zero upwards in the successive subfigures. When $\mathrm{Rb} = 0$ we have Newtonian flow which is quite strong, as evidenced by the deformation of the isotherms from the vertical alignment which corresponds to pure conduction. Of most interest in the present context is the large region in the centre of the cavity where there is a very slow circulation of fluid. Thus, when a weak yield threshold is introduced, as represented by $\mathrm{Rb} = 2$, a small stagnant region is formed right at the centre of the cavity. Apart from that, the flow and temperature fields are almost indistinguishable from their Newtonian counterparts.

Figure 3 near here

As Rb increases further, the stagnant region in the centre of the cavity grows quite rapidly and two new stagnant regions are formed at the top left and bottom right hand corners. When $\mathrm{Rb} = 15$ and above, the fluid motion becomes increasingly confined to a racetrack-like circuit around the edge of the cavity with a relatively large interior stagnant region. Although we have not quoted the values of $|\psi|_{\max}$ here, the decreasing strength of the convection as Rb increases may be deduced by the tendency of the isotherms to become less deformed and to tend back towards the vertical conduction state.

Finally, all four corner regions become stagnant and the central stagnant region continues to increase in size. When $\mathrm{Rb} = 24$ we see that the 'stagnant' region now includes some streamlines, even though we have increased c to 300 for this one case. This matter is discussed in detail in the Appendix, and it is a consequence of the fact that c is insufficiently large to give accurate streamlines this close to the cut-off value of Rb. However, the qualitative message that we are close to complete stagnation remains true, and the predicted Nusselt numbers are quite accurate, again as discussed in the Appendix.

We note that the cut-off value of Rb may be estimated to be roughly one quarter that of the chosen value of Ra. This is true for other values of Ra for a square cavity, but we do not include such Figures for the sake of brevity. Therefore it might be suggested that convection will take place whenever $\mathrm{Ra} > 4\mathrm{Rb}$. When $\mathrm{Rb} = 24$ in Fig. 3, the streamlines within the nonstagnant region are mostly almost vertical or almost horizontal, apart from close to teh corners, and therefore the network model developed in Rees (2015a) is of some relevance. In that chapter, the square porous cavity was assumed to consist of narrow vertical and horizontal channels of equal width which were arranged in a square network. It was shown analytically that convection arises only when $\mathrm{Ra} > 4\mathrm{Rb}$, precisely, and that fluid motion occurs only within the outermost circuit of that network. Then, as Ra increases, further circuits admit flow. These properties were shown to be caused by the strength of the buoyancy force compared with that required for the fluid to yield. The factor, 4, corresponds to the perimeter of the cavity in nondimensional terms. While the flow in the present problen is governed by an isotropic Darcy-Bingham law, the numerical evidence in Fig. 3 suggests that the same criterion for flow to arise might also apply here.

In Fig. 4 we fix the value of Rb at 10 and investigate the consequence of increasing the value of Ra. The first value of Ra is just above 4Rb and the flow is again confined to an outer circuit and the isotherms are almost vertical. We see that the evolution of the flow and temperature fields as Ra increases for fixed values of Rb mimics that found when reducing Rb for a fixed value of Ra. In both cases the value of $\mathrm{Ra} - 4\mathrm{Rb}$ is increasing, and this may be interpreted as an increasing effective buoyancy force.

Figure 4 near here

Figure 5 is concerned with a cavity having aspect ratio, $A = 2$ where $\mathrm{Rb} = 10$. In this case a network analysis of the type given in Rees (2015a) would suggest that convection takes place whenever Ra >

6Rb, where 6 is the length of the perimeter of the cavity. This certainly appears to be consistent with the numerical results in Fig. 5 where the induced flow is confined mainly to narrow regions close to the boundaries when Ra = 65. As Ra increases, convection increases in strength and the size of the central stagnation region reduces. Even when Ra takes a modest increase from 65 to 70, the regions within which fluid flows increases in thickness quite markedly. However, the stagnation region remains of quite substantial area even when Ra is as large as 200. The Newtonian counterpart of this flow is well-known to exhibit parallel flow in the middle of the cavity (i.e. in the horizontal direction) once the aspect ratio is sufficiently large, and therefore it is to be expected that stagnant region of uniform vertical thickness will form in these circumstances. This is seen clearly in the cases, Ra = 150 and 200, where it may also be seen that the stagnant region slopes towards the leading edge of the thermal boundary layers on the vertical surfaces, and in the case shown in Fig. 6 which depicts convection in a cavity of aspect ratio, $A = 4$.

Figures 5 and 6 near here

Figure 7 shows the evolution of the flow and temperature fields for a cavity with aspect ratio, $A = ½$, where Rb = 10 once more. In this case convection arises when Ra > 3Rb, according to network modelling of the kind used in When Ra = 35, which is just above the convection threshold, the flow is confined yet again to narrow layers next the boundary of the cavity. While the thickness of the region of flow (say up the hot surface on the left) increases with Ra in this Figure, eventually narrow thermal boundary layers will form on the vertical surfaces and it is quite possible that the width of the stagnant region might increase once more when Ra is sufficiently large.

Figure 7 near here

3.2 The strength of the flow and the Nusselt number

Having seen how the flow and temperature fields evolve with Ra, Rb and A, we now summarise these flows in terms of the flow strength, which is given by $|\psi|_{\max}$, and the Nusselt number, Nu, which is defined according to

$$\mathrm{Nu} = -\int_0^1 \left.\frac{\partial\theta}{\partial x}\right|_{x=0} dy. \tag{22}$$

When Ra = 0 the cavity admits a state of pure conduction where $\theta = 1 - x/A$, and therefore the Nusselt number is given by,

$$\mathrm{Nu}(\mathrm{Ra} = 0) = 1/A. \tag{23}$$

Figure 8 shows how both $|\psi|_{\max}$ and Nu vary with Ra up to the maximum value of 200. Curves are shown for Rb taking values which are multiples of 5 from 0 to 30. Attention is also confined to three different values of the aspect ratio, $A = 2$, 1 and ½. In all cases we have employed $c = 40$ as the regularisation constant; while it is possible to compute some cases for larger values (as given in Figs. 3 to 7), the present value is nevertheless quite large, gives excellent accuracy, and iterative convergence is generally quite robust.

Figure 8 near here

When Rb = 0 the Newtonian flow case is recovered and when Ra first increases from 0 then $|\psi|_{\max}$ increases linearly at first and Nu rises quadratically. When Rb takes nonzero values this well-known scenario changes. The detailed curves for both $|\psi|_{\max}$ and Nu show that values close to those of the conduction state are maintained almost perfectly until a threshold value of Ra is reached. Although we have already stated theoretical reasons for

$$\mathrm{Ra}_{\mathrm{threshold}} = (2 + 2A)\mathrm{Rb} \tag{24}$$

to be regarded as a perfect threshold value for convection to begin as Ra increases, it is not readily visible in Fig. 8. One reason for this is that the region within which convection takes place increases with Ra, which would immediately cause $|\psi|_{\max}$ to increase quadratically. The second reason is that the use of the regularisation causes a gradual increase in response, especially when Ra is close to the threshold value. The clear message from Fig. 8, then, is that while convection is enhanced as Ra increases it is progressively weakened as Rb increases. The balance between these two effects is governed by the value of Ra compared with that given in (24).

4 Conclusions

This paper describes the first set of computed convective flows within a porous medium when saturated by a Bingham fluid. An isotropic Darcy-Bingham law has been presented and approximated using a regularized model. Numerical solutions have been obtained for a a wide range of values of both Ra and Rb and for a selection of cavity aspect ratios. For a rectangular cavity we find that the fluid remains stagnant until an onset value of Ra is exceeded; this value depends linearly on both the value of Rb and the aspect ratio, A. Immediately post-onset the flow path takes the form of a narrow circuit near the outer boundary of the cavity, and this path widens as Ra increases. In general, the centre of the cavity and the four corner regions always remain stagnant whenever Rb is nonzero, but the size of the central stagnant region reduces in size as Ra increases.

The analysis contained in the Appendix was an essential preparation for a survey of parameter space. The usual protocol whereby, say, successive interval-halving is carried out in order to assess the accuracy of the computed solutions is not sufficient for Bingham fluids. A detailed discussion was given in the Appendix of the need to have a sufficiently large value of the regularization constant, c, and on how the numerical method responds to having such large values. In general a compromise is needed so that the Darcy-Bingham law is suitably well-approximated by the regularization without the need for having an excessive number of grid points merely to resolve the threshold region in the flow.

References

Balhoff, M.T., Thompson, K.E.: Modeling the steady flow of yield-stress fluids in packed beds. American Institute of Chemical Engineers Journal **50**, 3034–3048 (2004).

Barnes, H.A.: The yield stress – a review or '$\pi\alpha\nu\tau\alpha\ \rho\epsilon\iota$' – everything flows?. Journal of non-Newtonian Fluid Mechanics **81**, 133-178 (1999).

Baytaş, A.C., Pop, I.: Free convection in a square porous cavity using a thermal nonequilibrium model. International Journal of Thermal Sciences **41**, 861-870 (2002).

Blythe, P.A., Daniels, P.G., Simpkins, P.G.: Thermally driven cavity flows in porous media. I. The vertical boundary layer structure near the corners. Proc. Roy. Soc. London **A380**, 119-136 (1982).

Blythe, P.A., Daniels, P.G., Simpkins, P.G.: Thermal convection in a cavity filled with a porous medium: a classification of limiting behaviours. Int. J. Heat Mass Transfer **26**, 701-708 (1983).

Buckingham, E.: On Plastic Flow through Capillary Tubes. Proceedings American Society for Testing Materials **21**, 1154-1156 (1921).

Celli, M.: Non-homogeneous model for a side heated square cavity filled with a nanofluid. International Journal of Heat and Fluid Flow **44**, 327-335 (2013).

Fahs, M., Younis, A., Makradi, A.: A reference benchmark solution for free convection in a square cavity filled with a heterogeneous porous medium. Numerical Heat Transfer Part B – Fundamentals **67**,

437-462 (2015).

Gill, A.E.: A proof that convection in a porous vertical slab is stable. Journal of Fluid Mechanics **35**, 545-547 (1969).

Jeong, S.W.: Determining the viscosity and yield surface of marine sediments using modified Bingham models. Geosciences Journal **17(3)**, 241–247 (2013).

Lai, F.C., Kulacki, F.A.: Natural convection across a vertical layered porous cavity. International Journal of Heat and Mass Transfer **31**, 1247-1260 (1988).

Lewis, S., Bassom, A.P., Rees, D.A.S.: The stability of vertical thermal boundary layer flow in a porous medium. European Journal of Mechanics B: Fluids **14**, 395-408 (1995).

Liu, H., Wang, J., Xie, Y., Ma, D., Shi, X.: Flow characteristics of heavy oil through porous media. Energy sources Part A . Recovery Utilization and Environmental Effects **34**, 347-359 (2012).

Maßmeyer, A.: Thermal instabilities in a yield-stress fluid: from the laboratory to the planetary scale. PhD thesis. Université Paris Sud. (2013).

Nash, S.: Investigating the flow behaviours of Bingham fluids in porous media. Final year MEng project report supervised by Dr. D.A.S.Rees, Department of Mechanical Engineering, University of Bath, Bath, U.K. (2013).

O'Donovan, E.J., Tanner, R.I.: Numerical study of the Bingham squeeze film problem. J. Non-Newtonian Fluid Mech. **15**, 75-83 (1984).

Pascal, H.: Nonsteady flow through porous media in the presence of a threshold gradient. Acta Mechanica **39**, 207–224 (1981).

Rees, D.A.S.: Convection of a Bingham fluid in a porous medium. Chapter 17. Handbook of Porous Media Volume III (ed. K.Vafai) Taylor and Francis (2015a).

Rees, D.A.S.: On convective boundary layer flows of a Bingham fluid in a porous medium. International Journal of Heat and Mass Transfer **82**, 206-212 (2015b).

Saeid, N.H., Pop, I.: Non-Darcy natural convection in a square cavity filled with a porous medium. Fluid Dynamics Research **36**, 35-43 (2005).

Shenoy, A.V.: Non-Newtonian fluid heat transfer. Advances in Heat Transfer **24**, 102-190 (1991).

Sochi, T., Blunt, M.J.: Pore-scale network modeling of Ellis and Herschel-Bulkley fluids. Journal of Petroleum Science and Engineering **60**, 105–124 (2008).

Turan, O., Poole, R.J., Chakraborty. N.: Aspect ratio effects in laminar natural convection of Bingham fluids in rectangular enclosures with differentially heated side walls. Journal of Non-Newtonian Fluid Mechanics **166**, 208-230 (2011).

Turan, O., Poole, R.J., Chakraborty, N.: Influences of boundary conditions on laminar natural convection of Bingham fluids in rectangular enclosures with differentially heated side walls. Heat Transfer Engineering **35 (9)**, 822-849 (2014).

Appendix

The aim of this appendix is to justify the present choices of the regularization constant, c, which appears in Eq. (12), and the numerical grid used for the computations.

Figure 9 displays the variation of both $|\psi|_{\max}$ and Nu with c for a square cavity with the relatively large Darcy-Rayleigh number, Ra = 150, and with Rb = 20. Different $N \times N$ grids have been used, where the values of N are given in the caption.

Figure 9 near here

When c takes a zero value we recover Newtonian flow. When c increases this causes (i) the threshold model to be approximated increasingly closely, and (ii) the effective viscosity to be increasingly large in what ought to be the unyielded zones. Therefore, for all values of N we see both $|\psi|_{\max}$ and Nu decreasing when c first increases from zero. However, each curve eventually achieves a minimum and then begins to rise, but the value of c at which this happens depends strongly on the grid resolution. We believe that the minimum signifies roughly when the chosen grid is beginning to struggle to resolve well the regularized approximation to the strict threshold model. That this is so is confirmed by the fact that the minimum arises at larger values of c when the grid becomes finer (cf. Fig. 9).

The black dots in Fig. 9 allow us to assess the absolute accuracy of our solutions. The numerical method is of second order accuracy, and therefore successive interval-halving should reduce the absolute error by a factor of 4. Therefore the distance between the black dots for $N = 32$ and $N = 64$ should be roughly 3 times that between $N = 64$ and $N = 128$, which is what is found.

Figure 10 shows how different values of c affect the variation with Ra of $|\psi|_{\max}$ and Nu when $\mathrm{Rb} = 20$. The different slopes of the $|\psi|_{\max}$ curve near to $\mathrm{Ra} = 0$ correspond to the slope of the $c = 0$ curve divided by $(1 + c)$ because the induced flow is still a linear response to the conduction temperature profile. But we see that there is very little difference between the curves for $c = 50$ and $c = 100$, and that the worst comparison is near to the threshold value, $\mathrm{Ra} = 80$.

Figure 10 near here

A just-post-onset case is presented in Fig. 11 where we see the effect of different values of c on the streamlines, isotherms and the predicted stagnation region when $\mathrm{Ra} = 100$ and $\mathrm{Rb} = 20$. The larger two values of c are almost indistinguishable in terms of the isotherm and the stagnation regions, although some streamlines are present in the stagnation region when $c = 40$. When c takes smaller values, the number of streamlines increases, and when $c = 10$ even the stagnation region is predicted incorrectly. Therefore, in general, it seems that c ought to be chosen to be sufficiently large that the ingress of streamlines into the predicted stagnation region is to be avoided.

Figure 11 near here

To summarise, we see that there must be a trade-off between the chosen value of c and the execution time of the code. An accurate approximation to the threshold model requires c to be as large as possible, but too large a value will always eventually degrade the solution even on what is a highly accurate grid for Newtonian flow. A good combination of c and N would seem, therefore, to correspond to a flat section near the minimum of one of these curves. Therefore we would recommend that computations of the kind shown in Fig. 9 be undertaken for any new configuration in order to determine suitable values of c. Therefore in Fig. 8 we use $c = 40$ and a steplength of $1/96$, which means that the unit square uses a 96×96 mesh. In the earlier Figures (3 to 7) we have generally used $c = 100$ which improves the behaviour of teh streamlines, although this increased value of c has very little effect on either $|\psi|_{\max}$ or Nu.

Figures

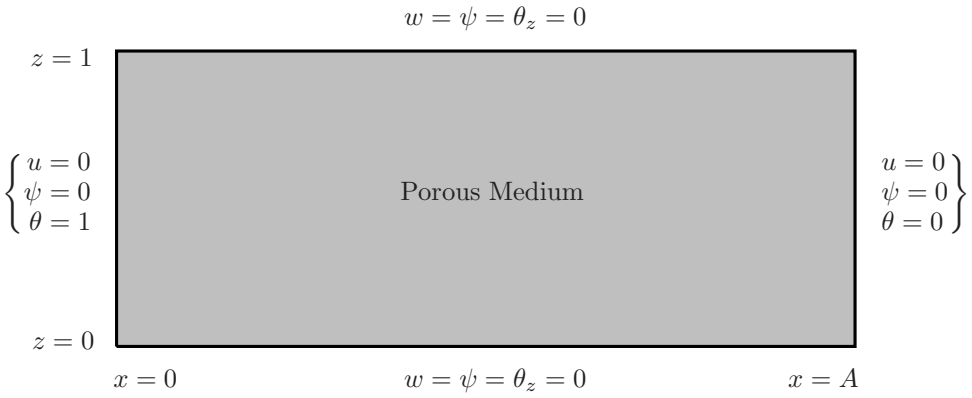

Figure 1. The porous cavity which is saturated by a Bingham fluid. The dimensions of the cavity and its boundary conditions are given in nondimensional form.

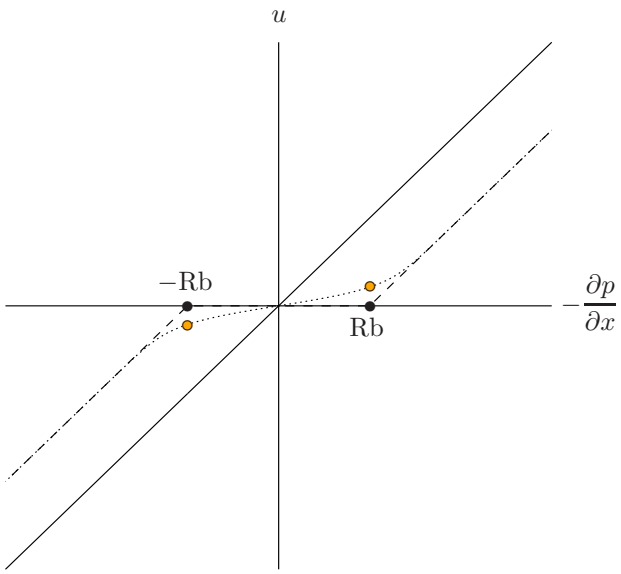

Figure 2. Showing the velocity/pressure gradient relationship for Darcy's law (continuous), the Pascal's (1981) threshold model (dashed), and the present regularized form of the threshold model (dotted) which corresponds to $c = 5$. The range of pressure gradient between the black disks corresponds to a stagnant medium. The orange circles indicate the range of velocities for the regularized model within which stagnation is deemed to occur.

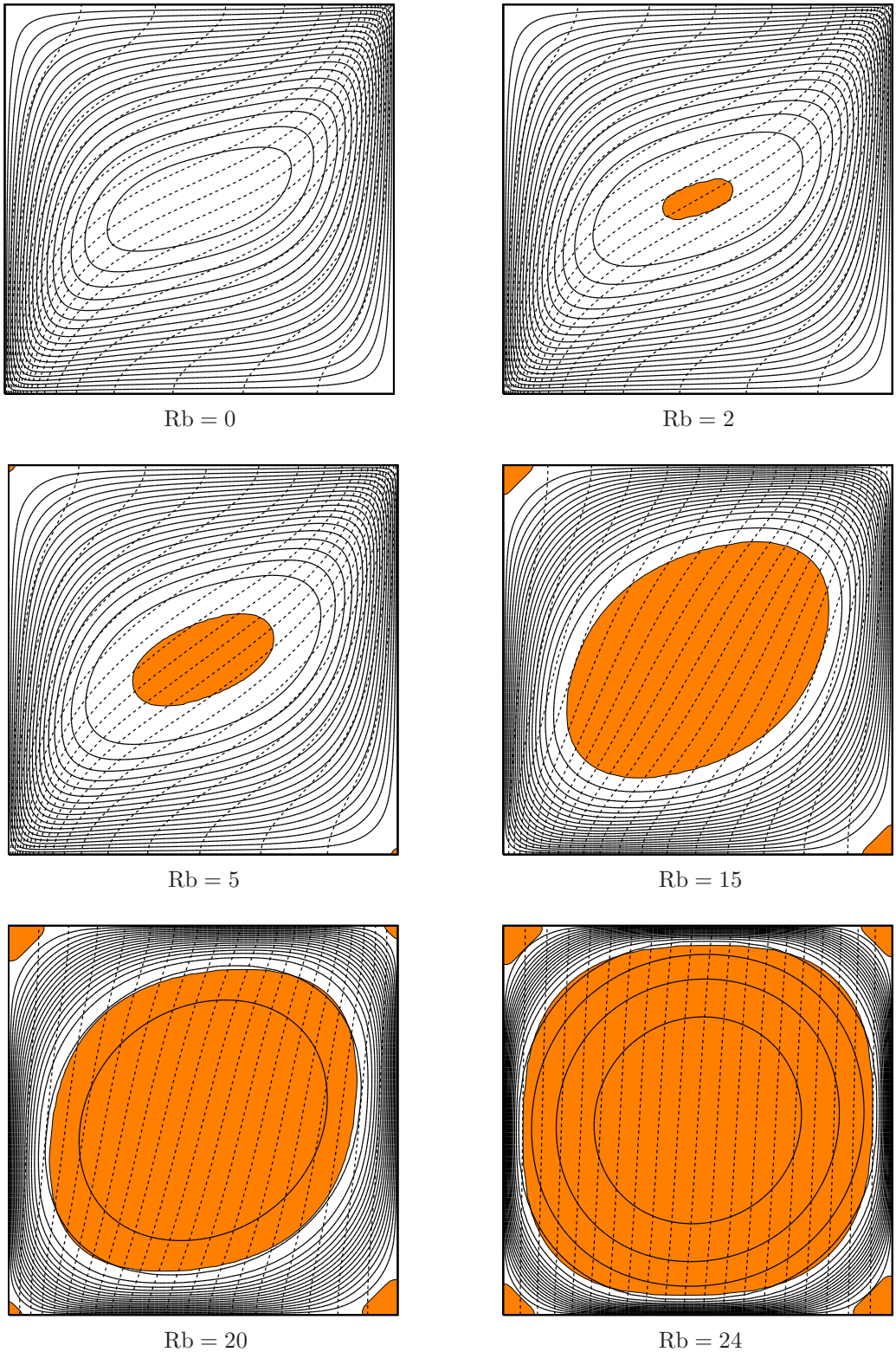

Figure 3. Showing the streamlines (continuous) and isotherms (dashed) for a unit square with Ra = 100 and $c = 100$, and for Rb taking the indicated values (but with $c = 300$ when Rb = 24). A 96×96 grid was used (except for Rb = 2 where it was 192×192). In each case the predicted stagnation region is shaded in orange and 20 equal intervals are taken for the respective isolines; these conventions apply to all other Figures of this type.

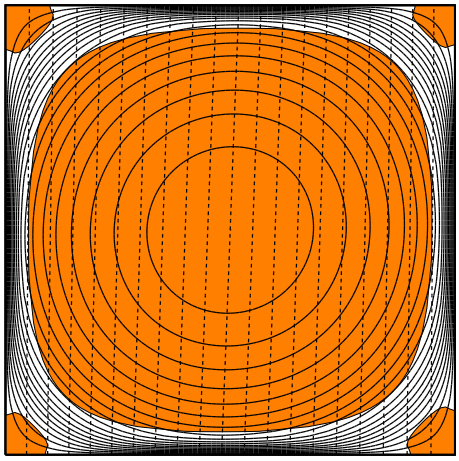

Ra = 42

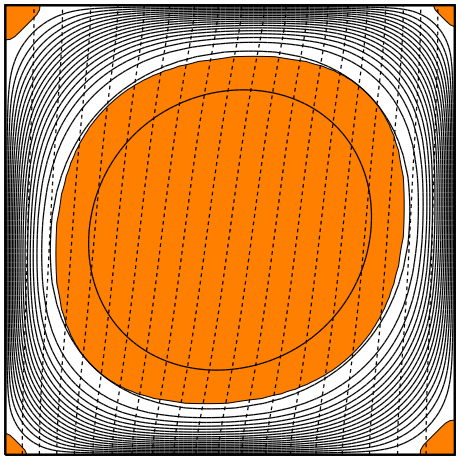

Ra = 50

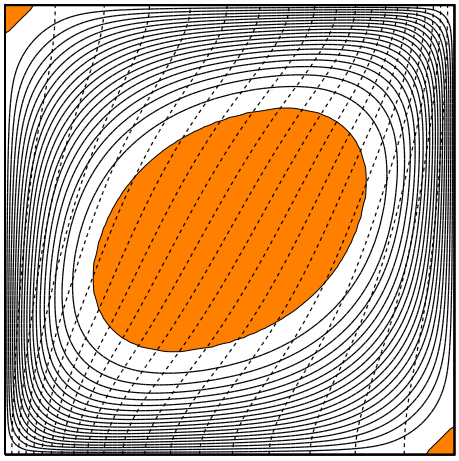

Ra = 75

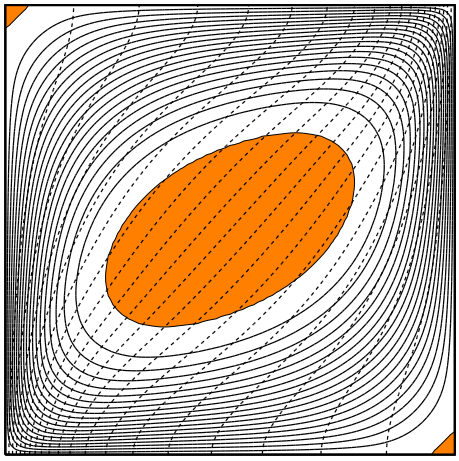

Ra = 100

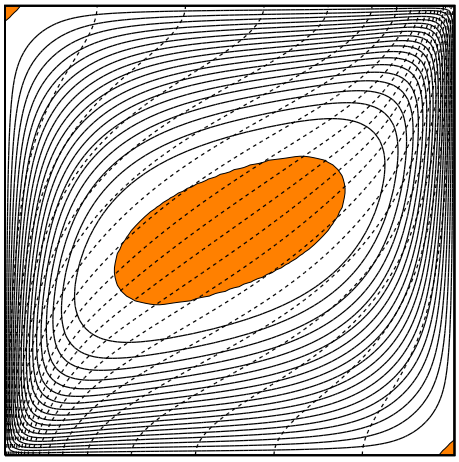

Ra = 150

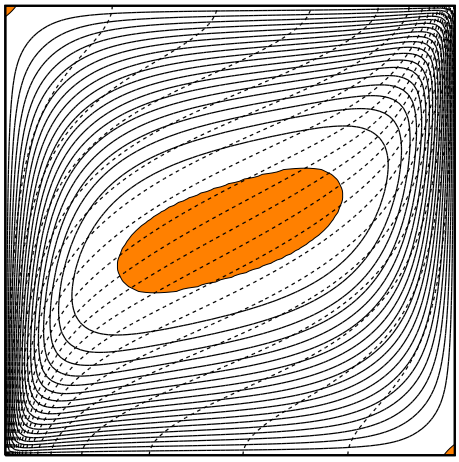

Ra = 200

Figure 4. Showing the streamlines (continuous) and isotherms (dashed) for a unit square with Rb = 10 and $c = 100$, and for Ra taking the indicated values. A 96×96 grid was used.

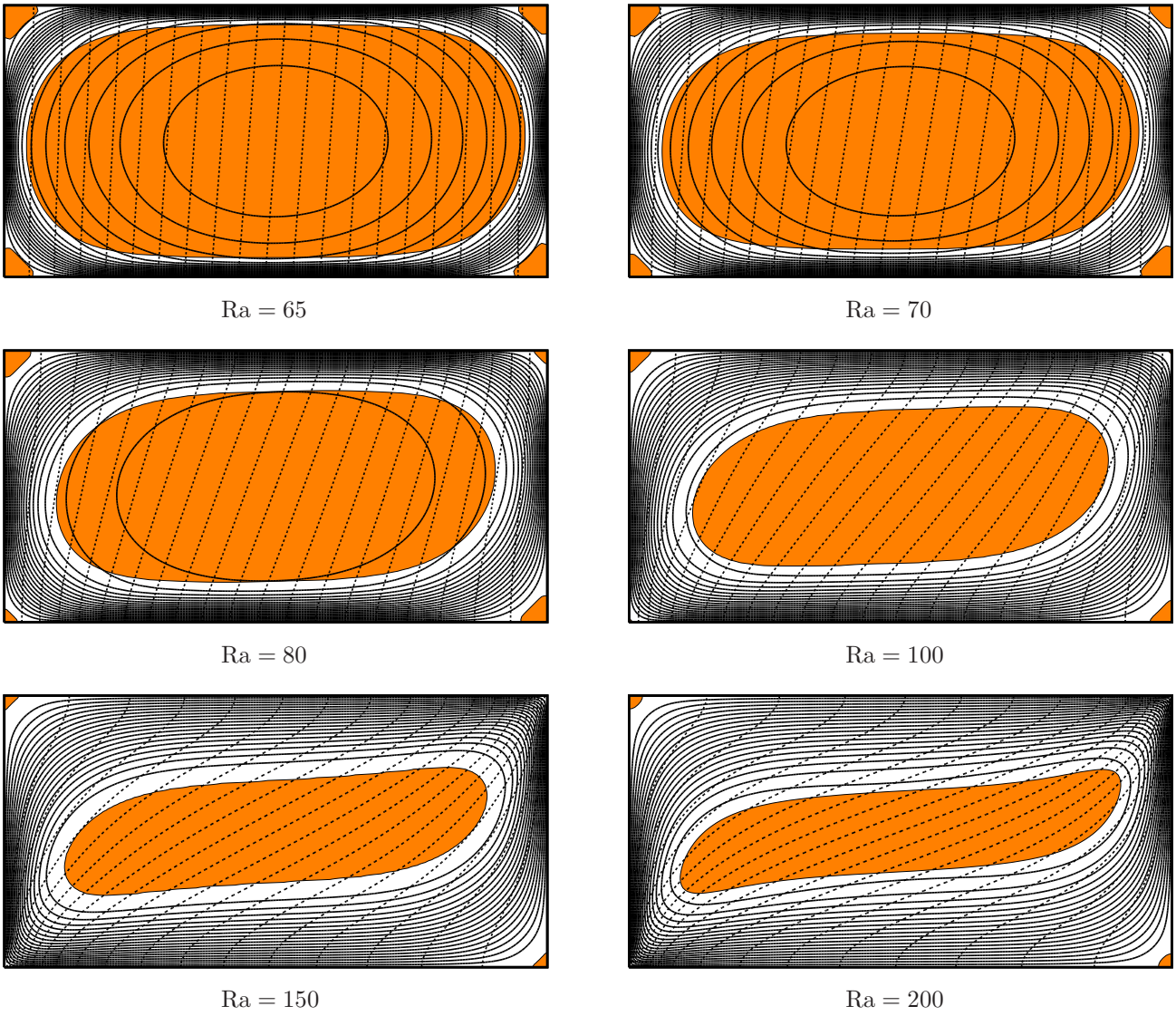

Figure 5. Showing the streamlines (continuous) and isotherms (dashed) for Rb = 10 with $c = 100$ for a cavity with aspect ratio, $A = 2$, and for Ra taking the indicated values. The case Rb = 65 uses $c = 200$. A 192×96 grid was used.

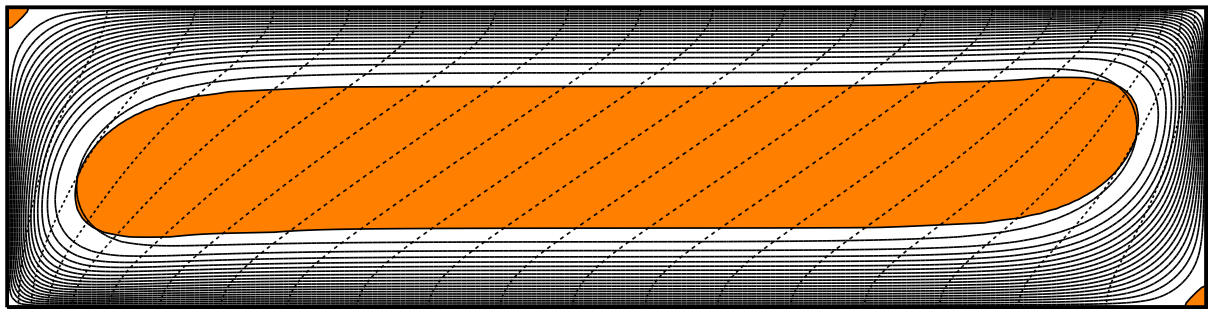

Figure 6. Showing the streamlines (continuous) and isotherms (dashed) for Ra = 200, Rb = 10 with $c = 100$ for a cavity with aspect ratio, $A = 4$. A 256×64 grid was used.

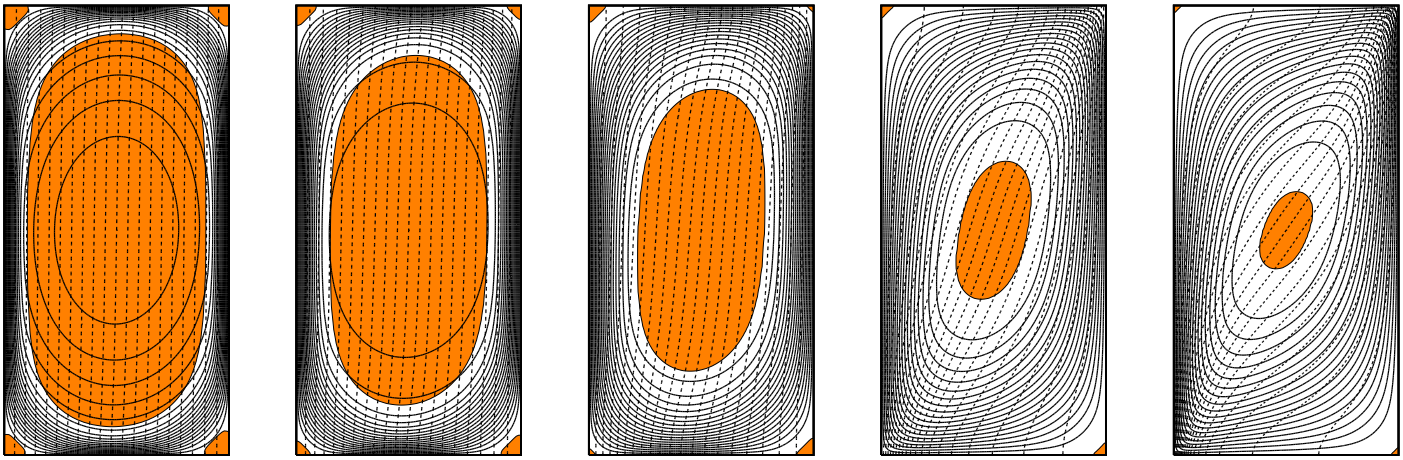

Figure 7. Showing the streamlines (continuous) and isotherms (dashed) for Rb = 10 with $c = 100$ for a cavity with aspect ratio, $A = ½$, and for Ra taking the indicated values. A 96×192 grid was used.

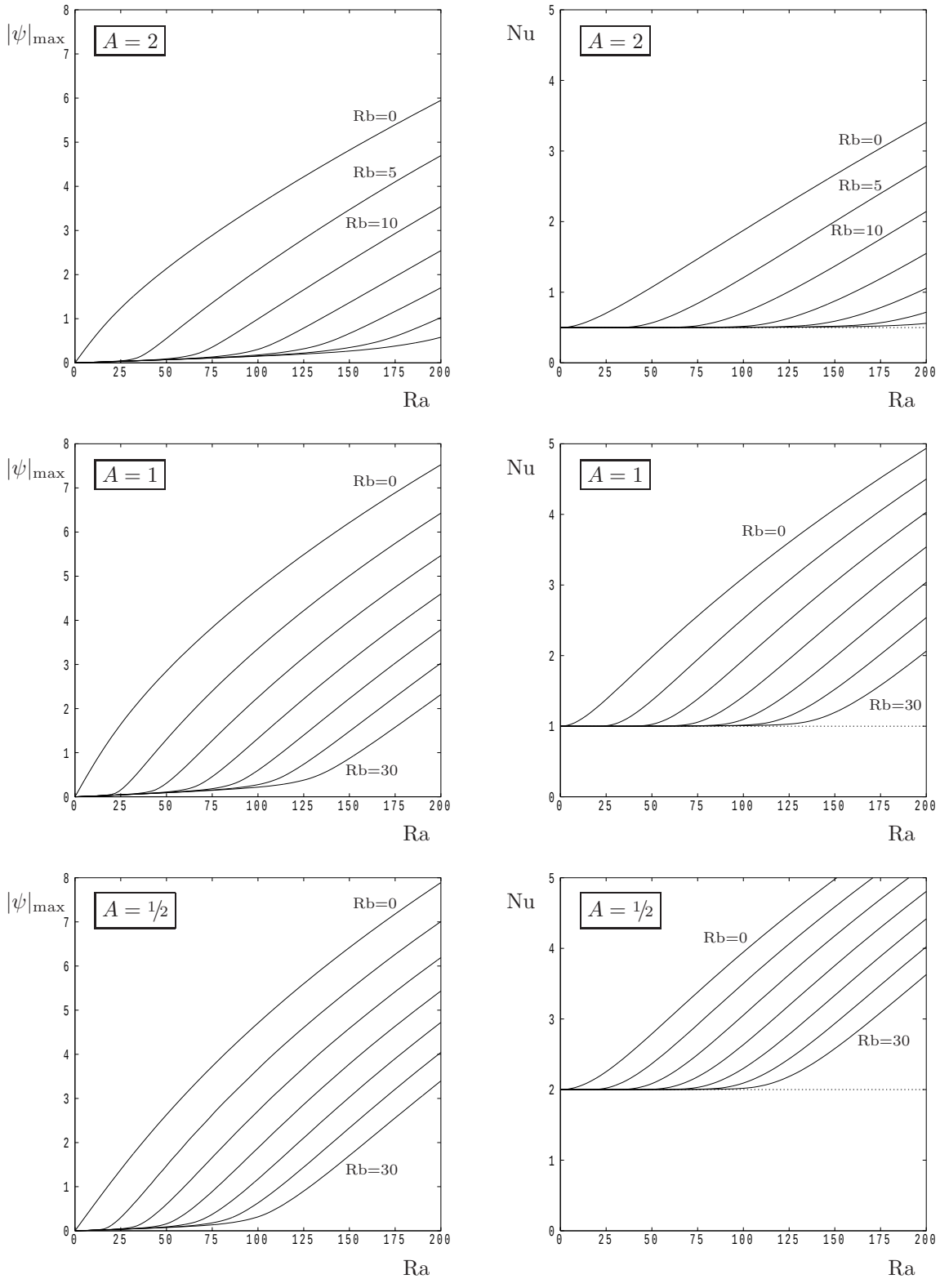

Figure 8. Showing the variation of both $|\psi|_{\max}$ and Nu with Ra for Rb = 0, 5, 10, $\cdots$, 30, for the three cases, $L = 2$, $L = 1$ and $L = 1/2$. The dashed line corresponds to the Nusselt number for the pure conduction profile.

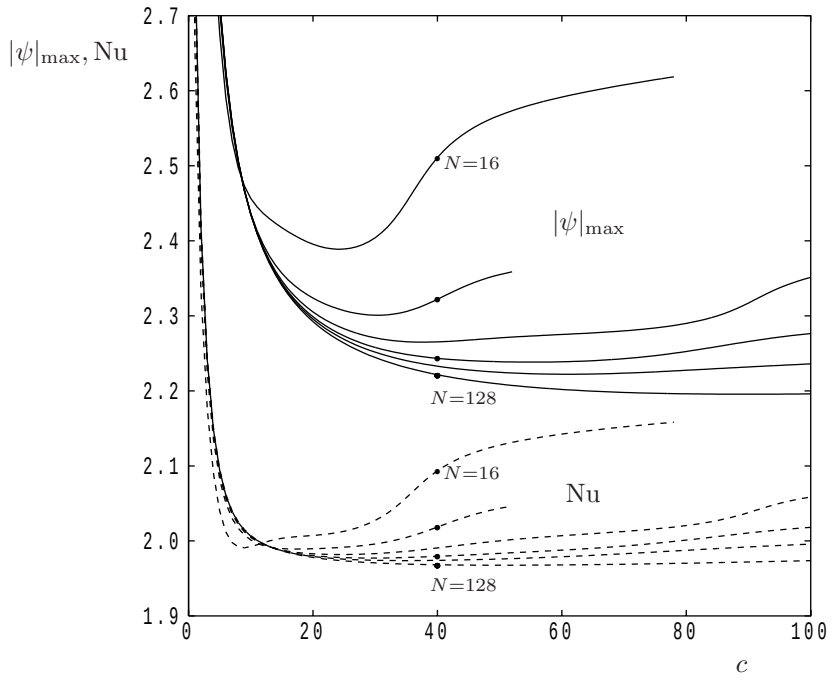

Figure 9: The variation of both $|\psi|_{\max}$ (solid lines) and Nu (dashed lines) with c for the case Ra = 150, Rb = 20 and $A = 1$ on an $N \times N$ grid where N = 16, 32, 48, 64, 80 and 128. The black circular disks indicate (from top to bottom) N = 16, 32, 64 and 128.

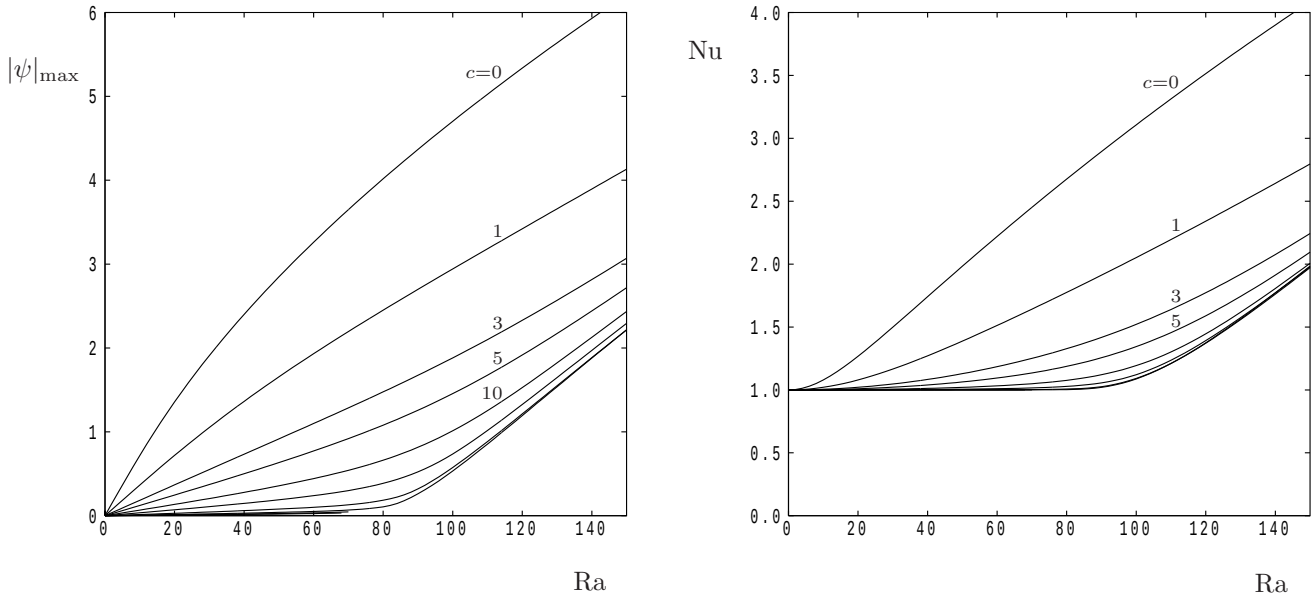

Figure 10. Showing that the variation of $|\psi|_{\max}$ and Nu with Ra on a 96×96 grid in a square cavity when Rb = 20 depends on the value of c in the regularization formula. Here c = 0, 1, 3, 5, 10, 20, 50, 100, 150 and 200.

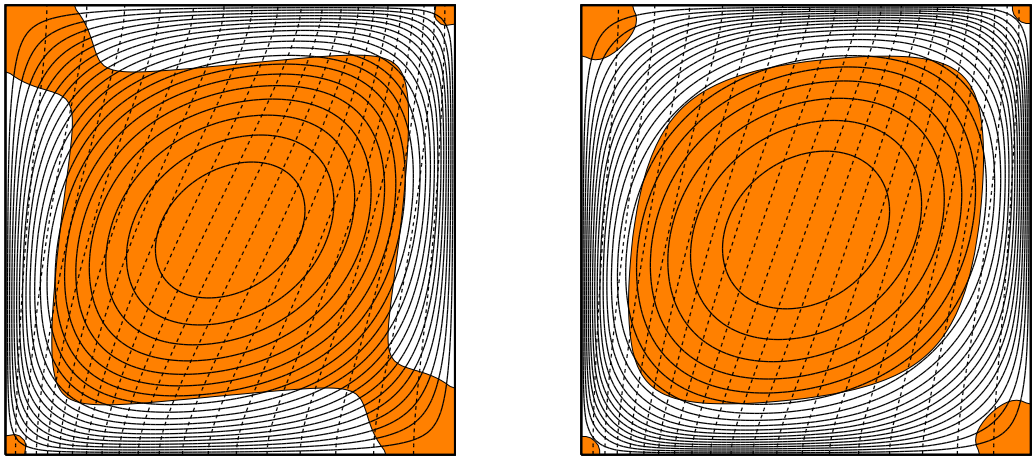

$c = 10$ $c = 20$

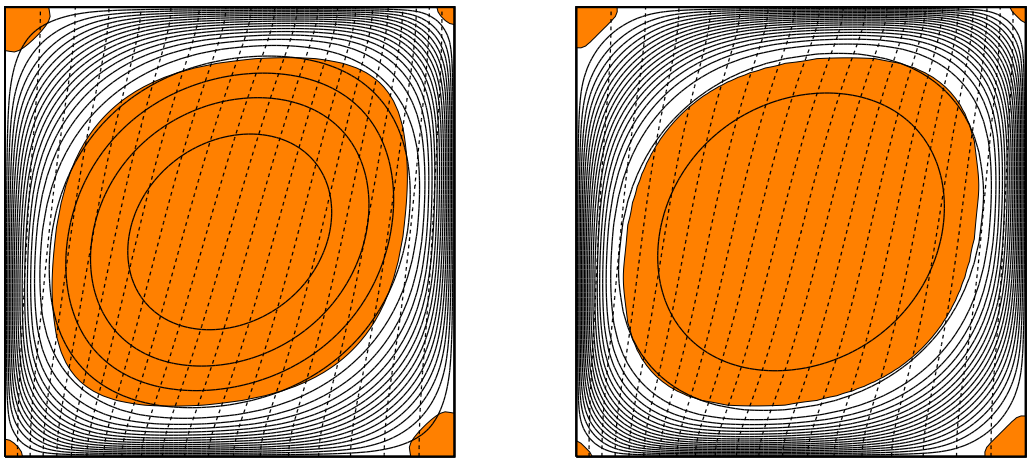

$c = 40$ $c = 100$

Figure 11. Showing the streamlines (continuous) and isotherms (dashed) for Ra = 100 and Rb = 20 for the following four values of c: 10, 20, 40 and 100. In each case the predicted stagnation region is shaded in orange.